Supporting Information

MEMS-Compatible, Gold Nanoisland Anchored 1D Aligned ZnO Heterojunction Nanofibers: Unveiling NO₂ Sensing Mechanism with *Operando* Photoluminescence Studies

Ramakrishnan Vishnuraj[a], Jayaseelan Dhakshinamoorthy[a], Keerthi G Nair[a], Mahaboobbatcha Aleem[a] and Biji Pullithadathil[a]*

*Corresponding author Email: bijuja123@yahoo.co.in; pbm@psgias.ac.in

S1 Electrospinning of pristine ZnO nanofibers:

Typically, 8 wt. % of polyvinyl Alcohol (PVA) was weighed and added in 10 mL of ultrapure water (Millipore Academic, Resistivity, 18.2 MΩ.cm) and kept for stirring at 45°C. After forming a viscous solution, 12 wt. % of zinc acetate was added slowly until homogeneity appeared. The solution was further stirred for 5 h after the addition of 1 mL ethanol. A clear transparent solution obtained was then subjected to electrospinning at a voltage, 18 kV with a feed rate of 0.2 mL/h. The $Zn(CH)_3COO_2$/PVA nanofibers were further annealed in a tubular furnace at 550°C for 4 h to obtain polycrystalline ZnO nanofibers.

S2 Synthesis of porous ZnO-GNI heterojunction nanorods:

0.2 g of ZnO nanorods was added to 10 mL of ethanol in a round bottom flask. 50μL of 0.14 mM of APTMS was added to round bottom flask containing ZnO nanorods to functionalization. After 12 h of stirring, the solution was centrifuged, washed and dried similar to the procedure followed for ZnO nanorods. 20mL of 2.5mM of $HAuCl_4$ and trisodium citrate was taken in a round bottom flask and stirred at ice cold condition. 0.2g of APTMS functionalized ZnO nanorods were added to the stirring mixture. To the stirring solution 0.6mL of 0.1 mM $NaBH_4$ was added finally and the colour changes from yellow to pink colour which indicates the formation of ZnO-GNI heterojunction nanorods. The material was centrifuged separately and washed several times using deionized water and ethanol and vacuum dried at 80°C for 5 h. The synthesised ZnO-GNI heterojunction nanorods were used for further studies after annealing at 550°C for 2 hr.
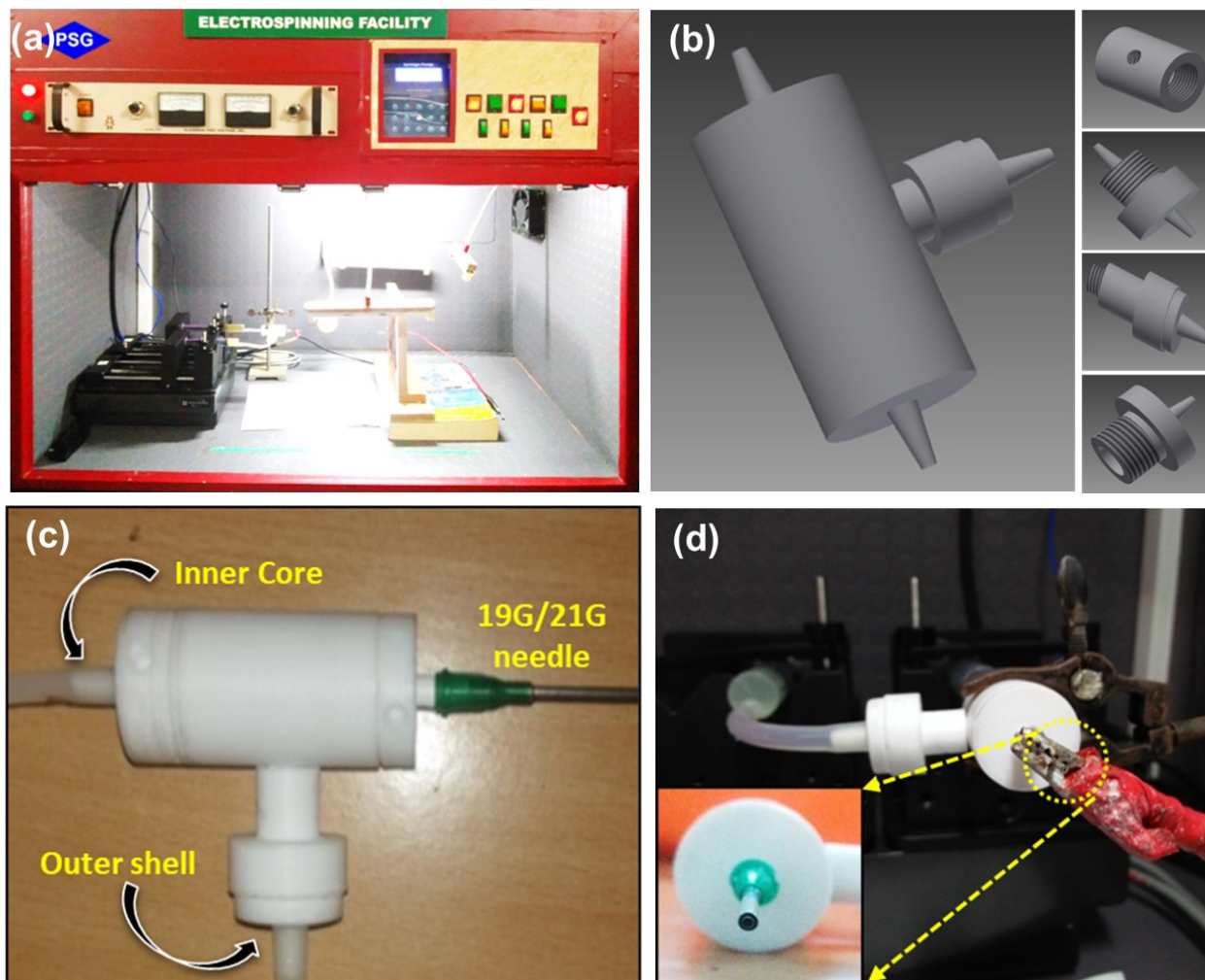
Figure S1 (a) Photograph of home-built Electrospinning unit with independently controlled dual syringe pumpalso with UV irradiation facility, (b) AutoCAD images of co-axial spinneret components (c-d) Photographs of the fabricated co-axial spinneret components fixed in the independent dual syringe pump (Inset show concentric arrangement of in/out needle).

S3 Characterization Techniques:

The ZnO-GNI heterojunction nanorods and nanofibers were spectroscopically and microscopically characterized by various techniques. Powder XRD patterns were acquired using Power X-ray diffractometer (Rigaku ULTIMA IV, Japan) using Cu Kα radiation of wavelength 1.5418 Å at a scanning rate of 0.02°/sec in the 2θ range of 20°–80°. Micro Raman studies for heterojunction ZnO-Au nanosystems were performed using confocal Raman microscope (WiTec, 300 Alpha, Germany) with He-Cd laser ($\lambda = 532$ nm) as the excitation light source and 1800 g/mm

gratings. The structure and morphology of the ZnO-GNI heterojunction nanofibers were examined using High-Resolution Transmission Electron Microscopy (JEOL JEM-2010, Japan) and Scanning Electron Microscopy (ZEISS EVO 18, US), with in-built energy-dispersive X-ray spectrometer (Oxford Instruments, INCA, UK). UV-DRS absorption spectra were acquired using JASCO UV (V-750) spectrophotometer. X-ray photoelectron spectroscopy (XPS) measurements were performed with a Phoibos 100 MCD Energy Analyser using monochromatized Al Kα excitation to analyse the chemical states of the materials and related defect studies. Operando solid state photoluminescence spectroscopic studies were performed using confocal Raman microscope (WiTec, 300 Alpha, Germany) with laser source ($\lambda = 355$ nm) and 1800 g/mm gratings. LINKAM probe station (HFS600E-PB4) equipped with a heating stage varying upto 600°C was used to perform the operando PL analysis during electrical measurements.

S4 Evaluation of gas sensor sensing properties:

Aligned ZnO-GNI HNFs were directly electrospun on gold IDA transducer electrodes using parallel plate collector which was further thermal treated at 550°C. The NO_2 sensing properties of ZnO-Au nanosystems were assessed using a custom-built gas sensor test station consisting of a stainless-steel double-walled test chamber having 5L of volume capacity which is equipped with Eurotherm temperature-controlled hot stage with temperature ranging from 0-600°C, sensor holder with highly conductive dual tungsten probes, 3 MFCs (0-1000 SLPM) for target gas dilution and the Agilent digital multimeter for data acquisition connected to a PC interfaced with Labview software. High pure N_2 gas was used as the carrier gas for NO_2 for specific concentration and the pressure was constantly maintained at 300sccm. Baratron 722B Absolute Capacitance Manometer (MKS Instruments, Singapore) was used to regulate the chamber pressure.

S5. Morphological analysis of porous ZnO nanorods:

TEM analysis was carried out for ZnO nanorods to infer about the structure and morphological characteristics. Figure S2(a-b) shows the TEM images of bare ZnO nanorods, where the uniform distribution of nanorods having length and width of 15 ± 0.5 μm and 150 ± 0.5 nm respectively were observed. Each nanorod extends to several micrometres with high aspect ratio as suited for electronics and sensing applications. **Figure S2(c)** shows the magnified image of ZnO nanorod and inset showing the SAED pattern of ZnO nanorods clearly implies the growth direction of ZnO

in *c*-axis with single crystalline nature. The SAED pattern were indexed and matching with the standard JCPDS data card no.65-3411. Figure S2(d) showing HR-TEM image of ZnO nanorods clearly shows the d-spacing value of 0.25 nm between the adjacent lattice planes corresponding to (100) plane lattice distance of hexagonal-wurtzite structured ZnO, indicating the growth direction along *c*-axis [0001].
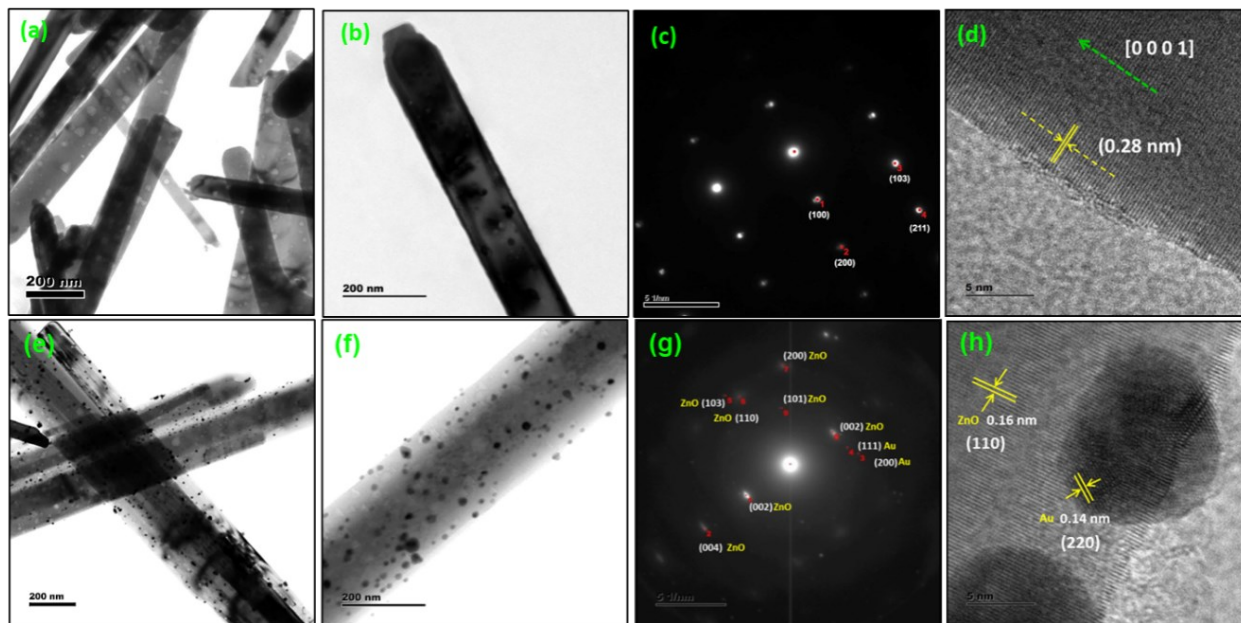
Figure S2 (a-b) TEM images of porous ZnO nanorods, (b) SAED pattern of ZnO nanorods, (c) the HRTEM image of ZnO nanorods, (e-f) TEM images of porous ZnO-GNI nanorods, (g) SAED pattern of ZnO-GNI nanorods, (h) the HRTEM image of ZnO-GNI nanorods.

Further, TEM image analysis of ZnO-GNI heterojunction nanorods are shown in the Figure S2(e-f). The Au nanoislands with an average particles size of 15 ± 2 nm were found to be uniformly anchored over the surface of ZnO nanorods which confirmed the formation of ZnO-GNI heterojunctions. Though ZnO and Au exhibited different exposed planes as (110) and (220) planes respectively, it must be noted that the interplanar spacing between (110) plane of ZnO and (220) plane of Au was found to be matching. SAED pattern of porous ZnO-GNI nanorods is shown in Figure S2(g), which clearly implies the growth direction of ZnO in *c*-axis with single crystalline nature. The HR-TEM images of the heterojunctions nanorods showed well-resolved interplanar distances corresponding to ZnO as $d(110) = 0.167$ Å with hexagonal-structure having growth direction along *c*-axis [001] and Au as $d(220) = 0.14$ Å shown in Figure S2(h).

## S6. XPS analysis of ZnO-GNI heterojunction nanorods:
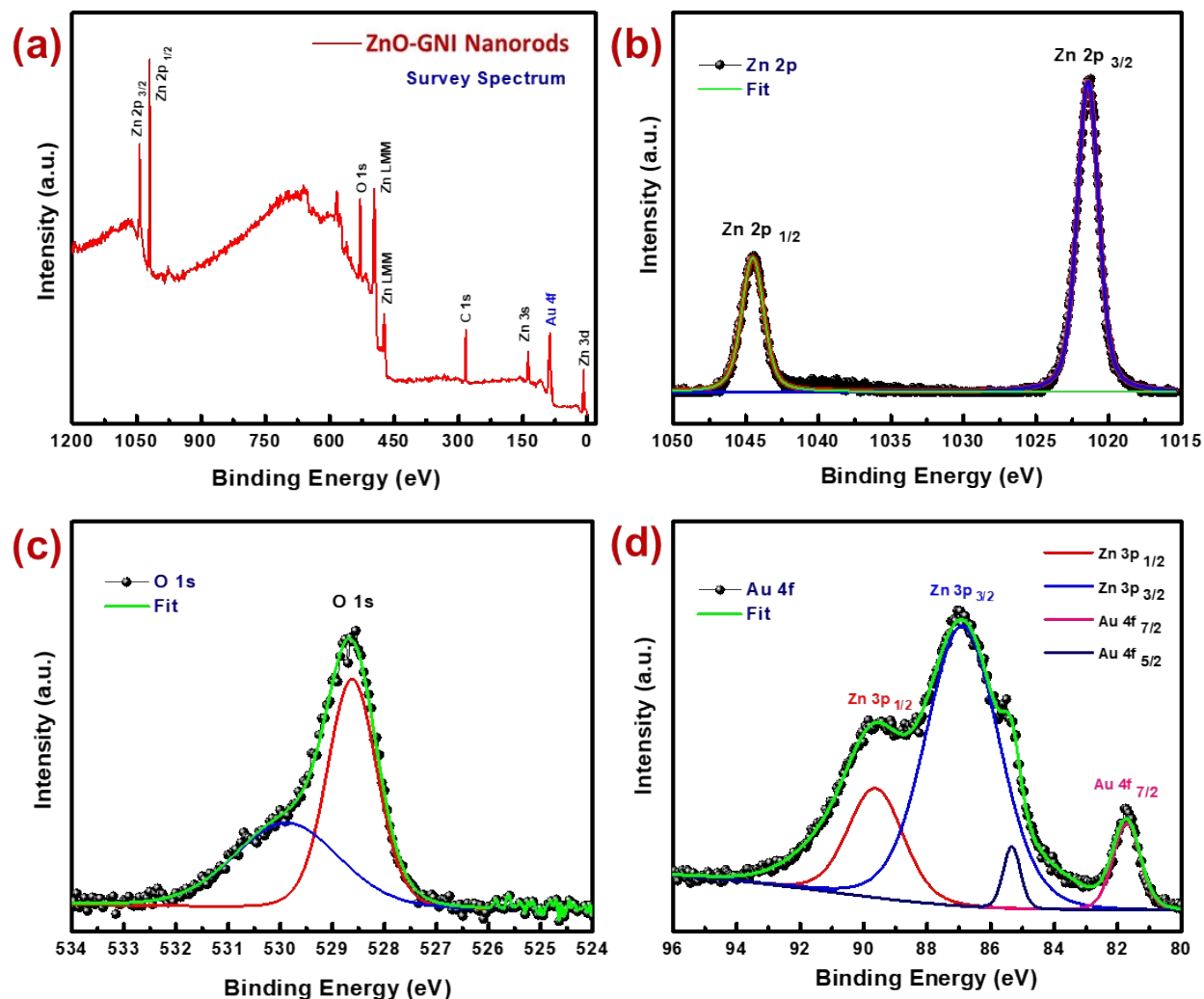
Figure S3 (a) Survey spectrum XPS analysis of pristine ZnO-GNI nanofibers (b) Zn 2p (c) O 1s and (d) Au 4f.

S7. UV–visible diffuses reflectance spectroscopy (DRS) analysis of ZnO-GNI heterojunction systems:

The band gap energy of the ZnO-GNI heterojunction systems is measured by the extrapolation of the linear portion of the graph between the modified Kubelka-Munk function $[F(R)*h\nu]^2$ versus photon energy (hν) shown in the inset **Figure S4(b)**.

$$F_{KM} = \frac{(1-R)^2}{2R} \qquad (S1)$$

The band gaps of the pristine porous 1D ZnO nanostructure and 1D heterojunction ZnO-GNI nanostructures were calculated shown in the table S1. The considerable change observed in the band gaps is due to the interfacial electron transfer between ZnO and Au nanocluster.
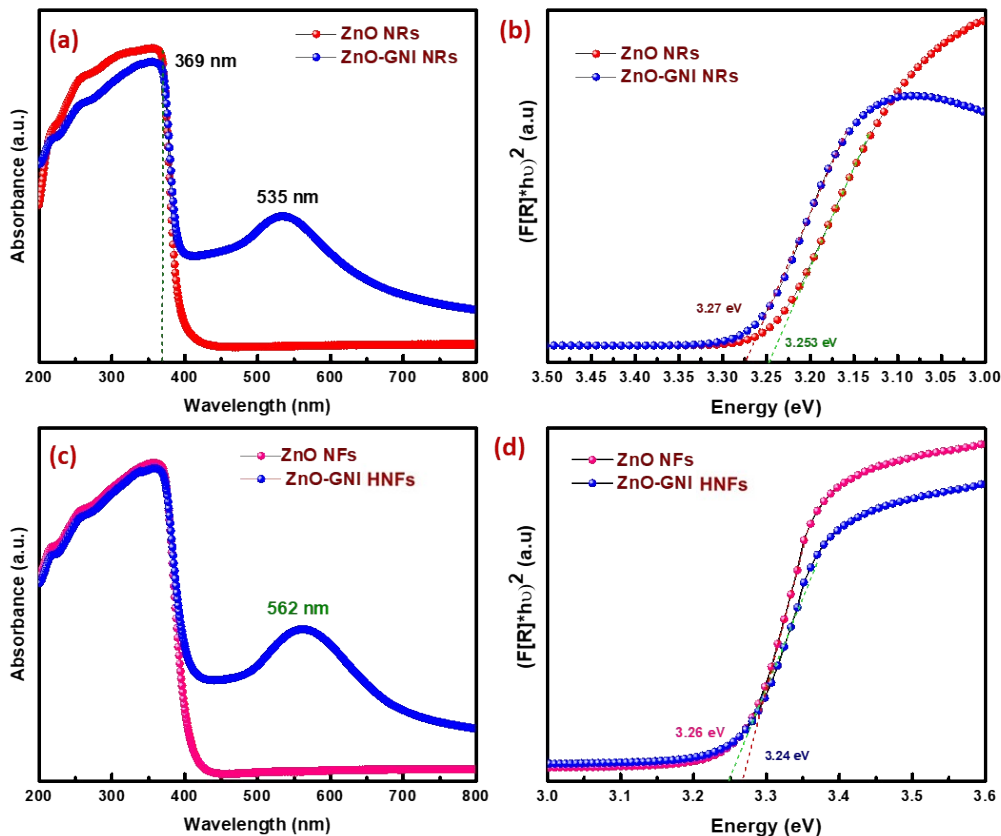

Figure S4 (a & c) UV–Vis DRS spectra of ZnO-GNI nanosystems. (b) Kubelka-Munk function versus energy plots of ZnO-GNI nanosystems.

Table S1. Estimation of Energy Bandgap of ZnO-GNI nanosystems:

Materials	Bandgap
ZnO nanorods	3.27 eV
ZnO-GNI nanorods	3.25 eV
ZnO nanofibers	3.26 eV
ZnO-GNI nanofibers	3.24 eV

Table S2. Mesh Statistics:

| Description	Value
Minimum element equality	1.95E-4
Average element equality	0.674
Tetrahedron	459549
Triangle	18383
Edge element	1527
Vertex element	152
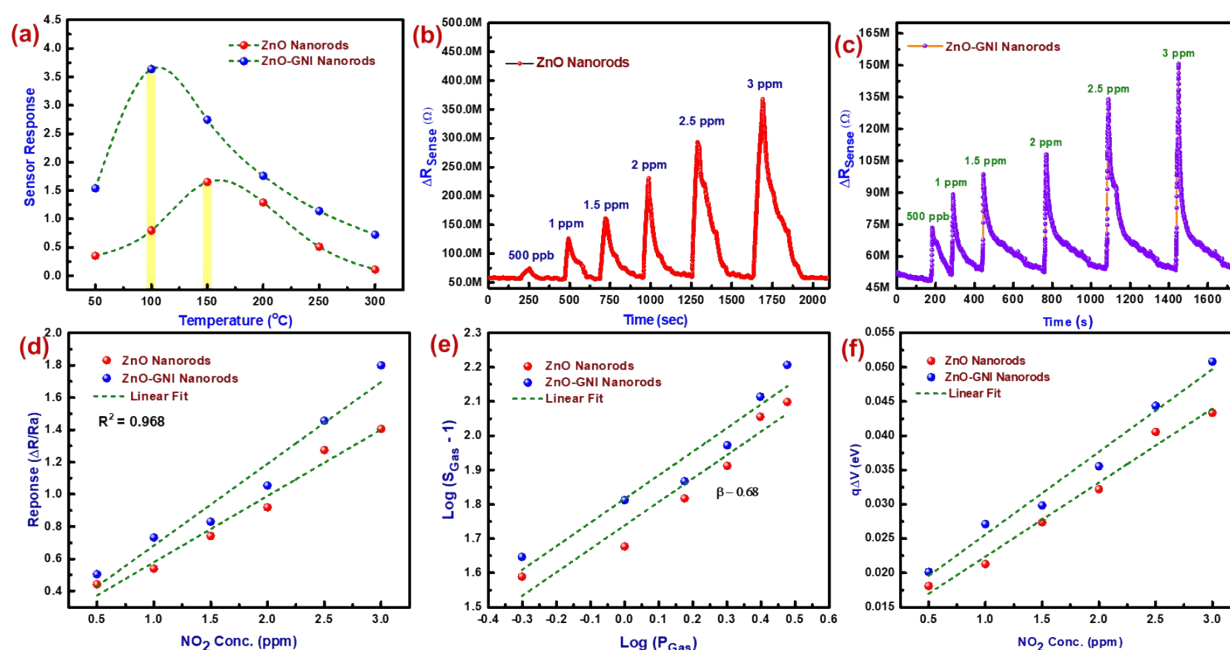
Figure S5 (a) Sensor response graph for 1 ppm of NO_2 gas as a function of temperature for ZnO nanorods and ZnO-GNI nanorods. **(b-c)** Dynamic sensor response and recovery graph of porous ZnO nanorods and ZnO-GNI nanorods at its operating temperature, **(d)** Sensor response versus NO_2 concentration (from 0.5 to 3 ppm) **(e)** log $(S_{gas} - 1)$ versus log(P_{gas}) plot toward $0.5 - 3$ ppm of NO_2 gas, **(f)** Changes in band bending $(q\Delta V)$ with increases in NO_2 concentration $(0.5 - 3$ ppm) at operating temperature.

Table: S3 Comparison of NO_2 gas sensing results:

| Conc. of NO$_2$ (ppm)	ZnO nanorods		ZnO-GNI nanorods		ZnO nanofibers		ZnO-GNI nanofibers	
	S%	$T_{Response}$(s)	S%	$T_{Response}$(s)	S%	$T_{Response}$(s)	S%	$T_{Response}$(s)
0.5	44	21.6	52	8	31	5	196	4.2
1	53	23.4	73	10	82	5	296	5.6
1.5	74	23.4	83	11	193	7	462	8.4
2	91	26.1	105	10	407	9	704	8.8
2.5	127	31.5	145	11	479	9	1044	8
3	140	32.4	179	13	548	10	1419	8.4

S8. *In-situ* electrical Characteristics of porous heterojunction ZnO-GNI nanosystems:
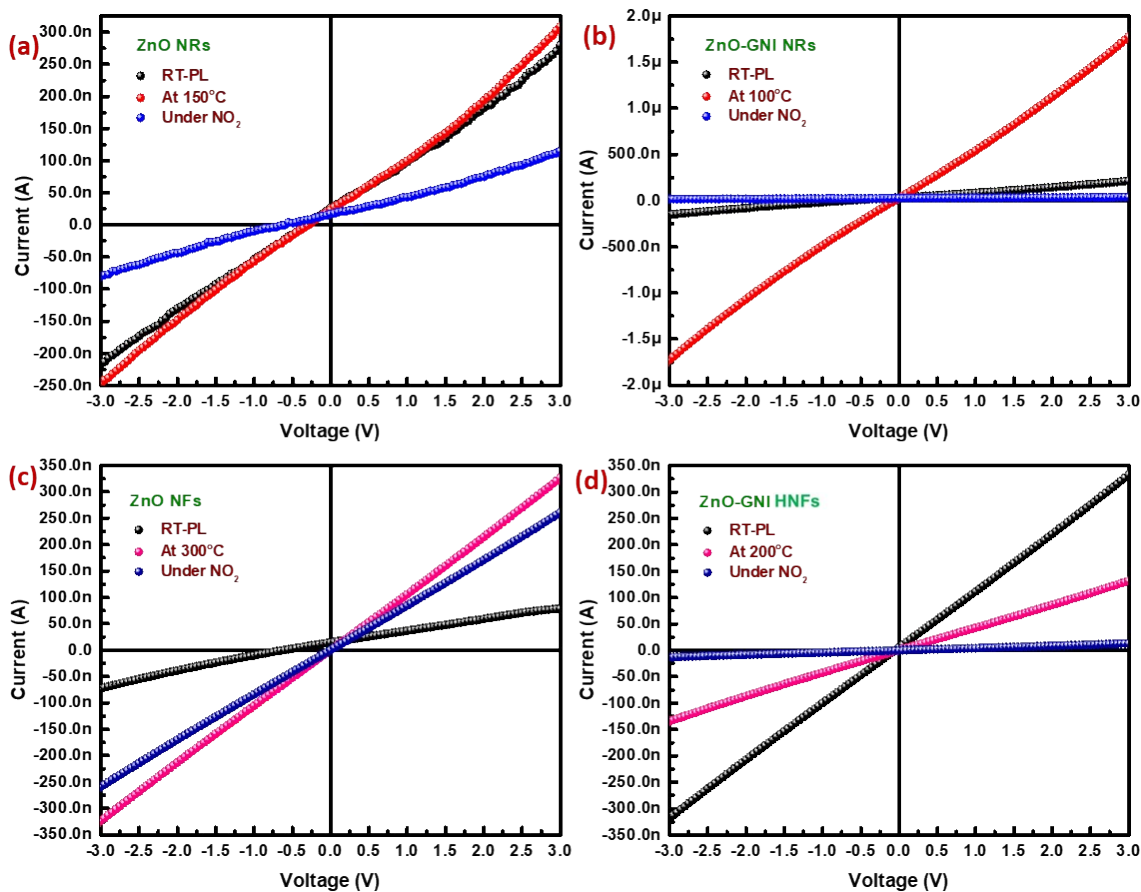
Figure S6 I-V graphs of (a) ZnO nanorods, (b) ZnO-GNI nanorods, (c) ZnO nanofibers and (d) ZnO-GNI nanofibers, taken in room temperature, operating temperature and during NO_2 exposure.

S9. *Operando* **photoluminescence spectroscopic analysis of ZnO and ZnO-GNI nanorods**:
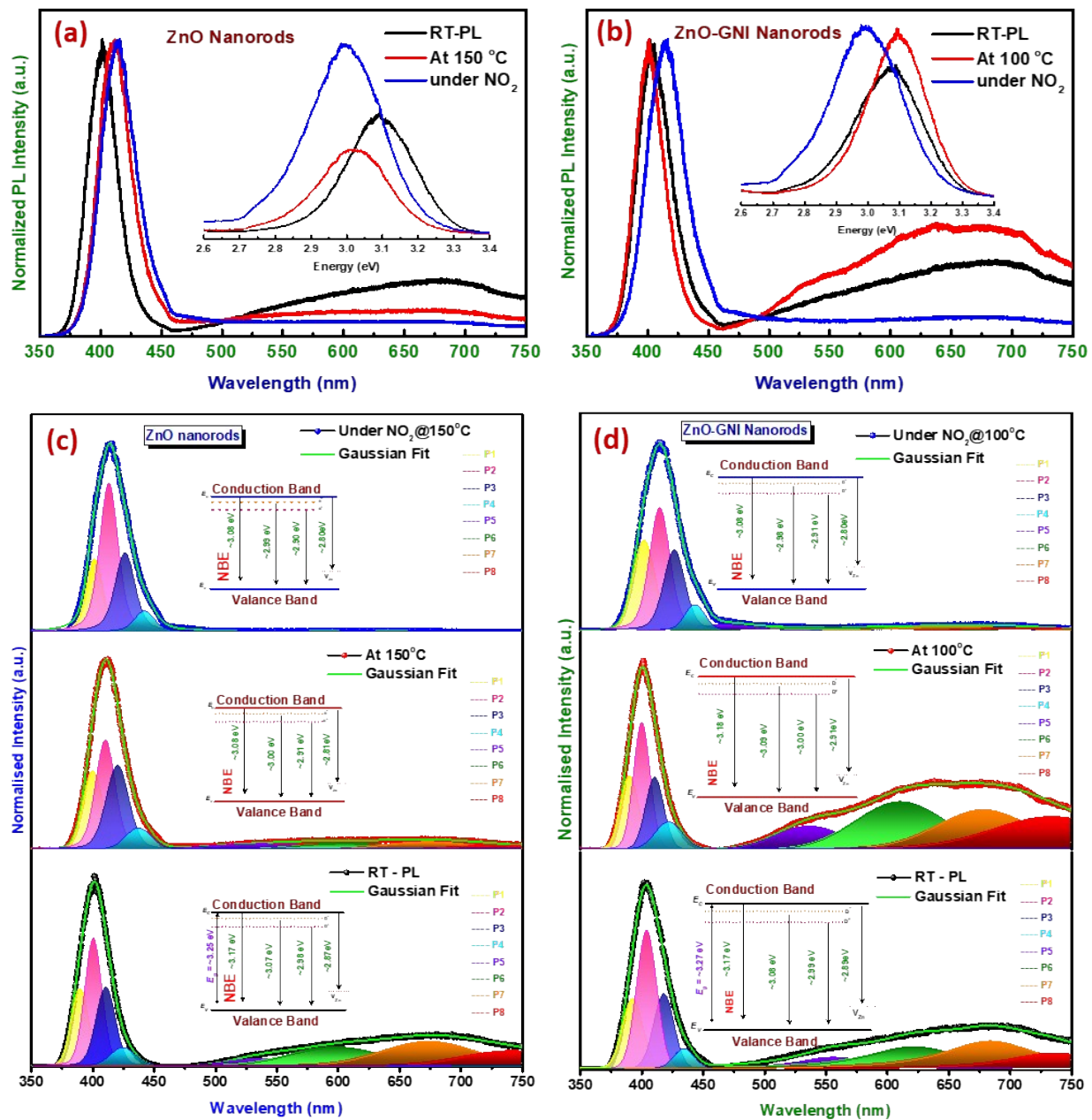
Figure S7. The *operando* PL spectra of **(a)** porous ZnO nanorods and **(b)** aligned ZnO-Au nanorods in ambient condition, operational condition and upon exposure on NO$_2$, comparison of Deconvoluted PL-NBE emission and DLs emission spectra of **(c)** ZnO nanorods and **(d)** ZnO-GNI nanorods. Various bands are fitted by Gaussian line shapes; Inset shows deep level energy diagram showing various defect states in the band gap of the materials.

Table S4 Details of the PL peaks (excitation wavelength 355 nm) fitted with Gaussian line shapes for the UV emission bands:

Code	Identity	ZnO nanorods			ZnO-GNI nanorods			ZnO nanofibers			ZnO-GNI nanofibers		
		RT-PL	150°C	NO$_2$	RT-PL	100°C	NO$_2$	RT-PL	300°C	NO$_2$	RT-PL	200°C	NO$_2$
P1	NBE	390.8	401.6	402.2	390.0	389.5	402.0	394.6	395.6	388.1	401.4	397.8	399.1
P2	ST to VB	402.8	412.8	414.0	401.9	400.6	415.5	405.5	406.1	396.7	414.9	409.1	413.7
P3	CB to O$_i$	415.3	425.9	426.2	414.5	412.5	426.0	417.4	417.5	404.9	430.6	422.3	425.6
P4	Zn$_i$ to V$_{Zn}$	430.6	441.1	442.6	428.7	425.9	442.1	433.9	432.2	414.6	449.4	447.7	443.7

Table S5 Comparison of the relative defect concentration (%) PL peaks fitted with Gaussian line shapes for the visible emission bands:

| Condition	Relative defect concentration (%)			
	ZnO nanorods	ZnO-GNI nanorods	ZnO nanofibers	ZnO-GNI nanofibers
Ambient Condition	53.1	66.6	54.6	56.2
Operating temperature	26.7	72.7	14.0	67.4
Under NO$_2$ exposure	2.3	16.9	2.4	48.4

S10. Cross selectivity of the gases:
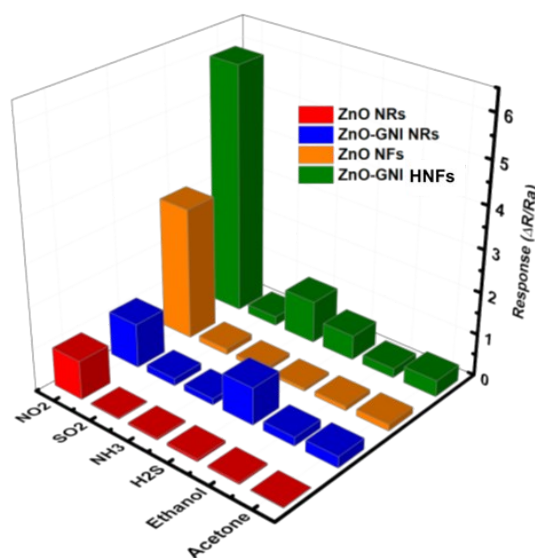
Figure S8 Cross selectivity studies of porous ZnO nanorods and nanofibers and porous heterojunction ZnO-GNI nanorods and nanofibers.
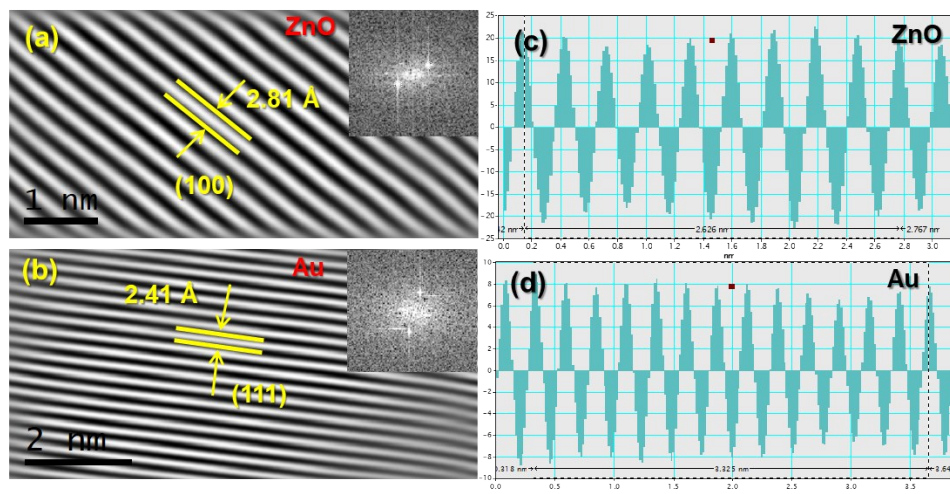
S11. Relative humidity interference studies:
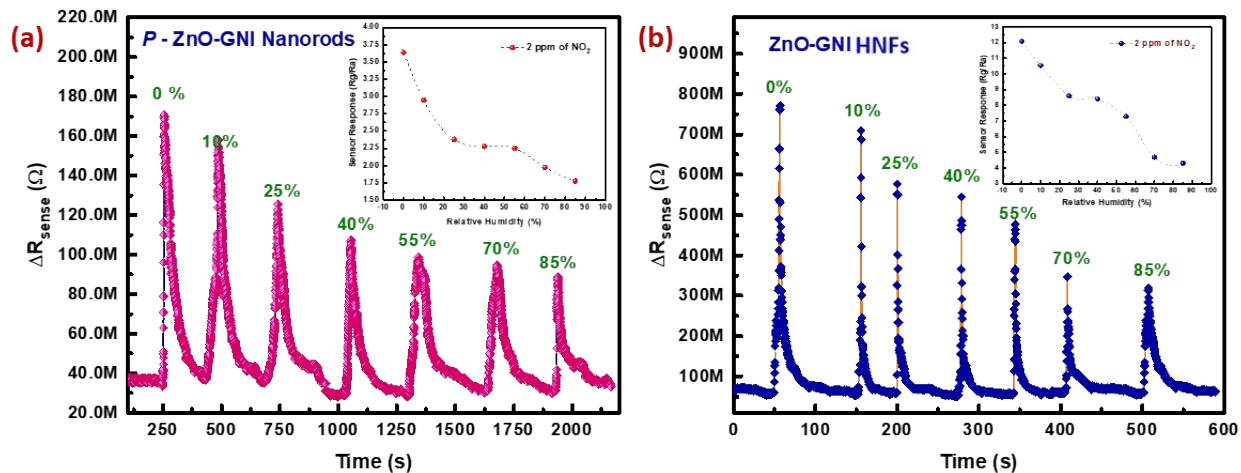
Figure S9. Relative humidity interference studies of ZnO-GNI heterojunction (a) porous ultra-long nanorods and (b) aligned nanofibers.

## S12. Repeatability and Stability studies:
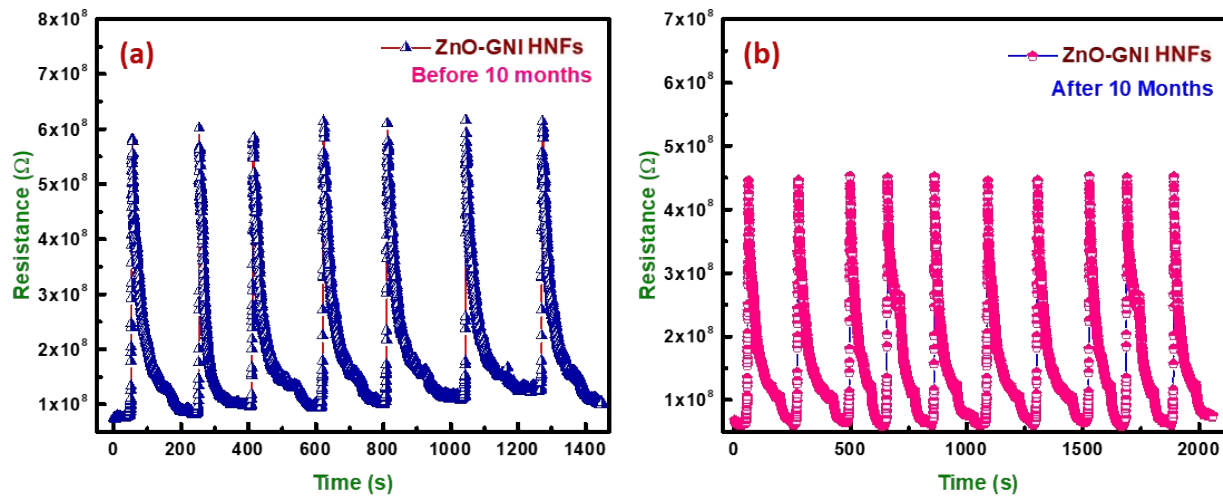
Figure S10. Repeatability and Stability studies of aligned ZnO-GNI HNFs (a) before 10 months and (b) after 10 months.

Figure S11 (a-b) inverse FFT images of ZnO and Au (inset showing the live FFT image of ZnO and Au) and (c-d) IFFT profile of ZnO and Au.

S13. BET Surface area analysis:

TEM analysis (**Figure 4a and S2a**) revealed the presence of mesoporous nature of the pristine ZnO and ZnO-GNI nanofibers which was further quantified by N_2 adsorption-desorption studies using BET Physisorption Analyzer as depicted in **Figure S12(a-b)**. The nitrogen adsorption-desorption isotherms of non-porous and porous pristine ZnO and ZnO-GNI HNFs are shown in **Figure S12(a)**.
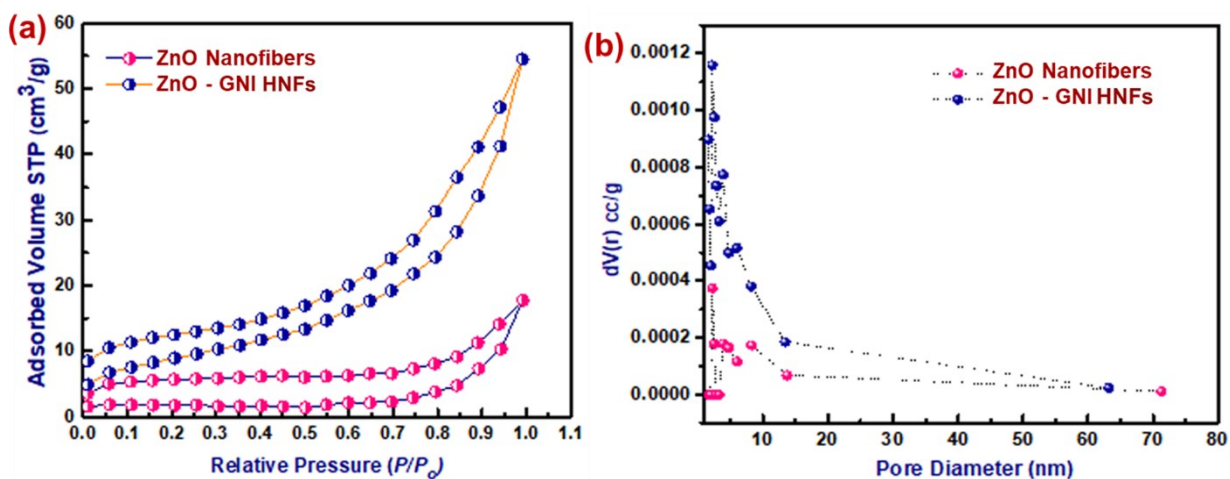

Figure S12 (a) Typical nitrogen adsorption–desorption isotherms of nonporous pristine ZnO and ZnO-GNI HNFs and (b) corresponding pore size distribution.

All materials exhibited typical type IV isotherms with the hysteresis loops at the P/P_0 ranging from 0.01 to 0.99, indicating the existence of mesoporous structure. The surface area, pore volume and pore size of ZnO-GNI heterojunction nanofibers were found to be significantly higher than that of pristine ZnO. However, BET curve of pristine ZnO and ZnO-GNI heterojunction nanofibers possessed I/IV type isotherm with H_4 hysteresis loop. The multilayer adsorption at low pressure region revealed the co-existence of micro and mesoporous structures. The formation of porous structure in nanofibers was mainly due to the decomposition of polymeric matrix at higher temperature, which leads to evolution of voids inside the nanofibers. Hence, the surface area and pore volume of heterojunction nanofibers were found to be predominantly increased compared to polycrystalline heterojunction nanorods. **Figure S12(b)** displays the corresponding pore size distribution derived from the non-local density functional theory (NLDFT) method. The pore size distribution of heterojunction nanosystems was found to be slightly reduced compared to bare ZnO, owing to the formation of Au nanoislands over the surface. The calculated BET surface area of pristine ZnO and porous ZnO-GNI heterojunction nanofibers are summarized in **Table S6**. The increase in specific surface area and pore volume can provide abundant surface-active sites and facilitate the easy charge-carrier transport leading to enhanced NO_2 sensing properties.

Table S6. Parameters estimated from BET analysis of bare pristine ZnO and ZnO-GNI HNFs.

Materials	Surface area (m²/g)	Pore volume (cm³/g)	Pore size (nm)
ZnO nanofiber	5.695	0.064	2.1547
ZnO-GNI heterojunction nanofiber	26.688	0.092	2.0146
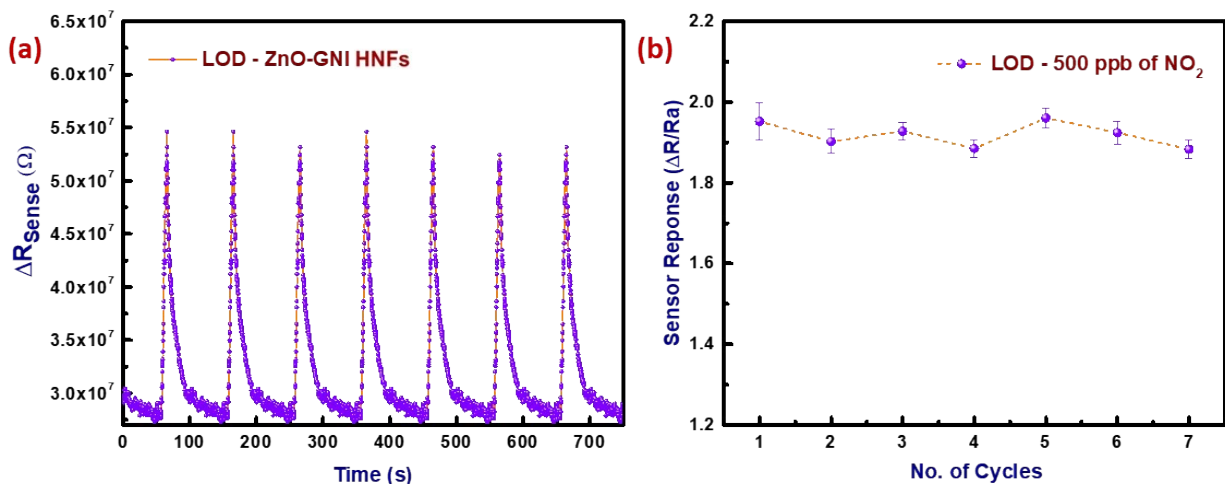
Figure S13 (a) Statistical temporal response of ZnO–GNI HNFs exposed to 500 ppb of NO_2 at its operating temperature (200°C) and (b) corresponding sensor response graph.

Table S7 Comparison of the NO_2 gas response to the presently fabricated aligned ZnO-GNI HNFs and the sensing materials reported in literatures.

Sensor materials	Fabrication method	Measuring range (ppm)	Operating temp.	Response (R_g/R_a)	Reference
ZnO nanorod/Au hybrids	Wet-chemical method	1-10 ppm	RT with with 532nm light illumination	4.66@1 ppm	1
ZnO@Au Micro-spheres	Chemical method	0.5-5 ppm	250°C	13.1@1ppm	2
ZnO NWs/Au NPs	Hydrothermal	1-20 ppm	150°C	31.4@1ppm	3
Au/ZnO thin films	Sol gel / spin coat	5 ppm	RT with UV radiance	0.6@5ppm	4
Au/ZnO sensor	Wet-chemical synthesis	2-6 ppm	RT with UV illumination	1.96@2ppm	5
ZnO/Au nanosheets	3-step synthesis	1-5 ppm	RT with UV irradiance	4.55@5ppm	6

Au/ZnO Nanorods	Hydrothermal /chemical method	5-50 ppm	300°C	4.14@50ppm	**7**
Aligned ZnO-GNI HNFs	Coaxial Electrospinning	0.5 – 3 ppm	200°C	14.19@3ppm	**Present Work**

References:

(1)   Wang, J.; Fan, S.; Xia, Y.; Yang, C.; Komarneni, S. Room-Temperature Gas Sensors Based on ZnO Nanorod/Au Hybrids: Visible-Light-Modulated Dual Selectivity to NO2 and NH3. *J. Hazard. Mater.* **2020**, *381* (February 2019), 120919.

(2)   Veeran Ponnuvelu, D.; Abdulla, S.; Pullithadathil, B. Highly Monodispersed Mesoporous, Heterojunction ZnO@Au Micro-Spheres for Trace-Level Detection of NO2 Gas. *Microporous Mesoporous Mater.* **2018**, *255*, 156–165.

(3)   Chen, X.; Shen, Y.; Zhong, X.; Li, T.; Zhao, S.; Zhou, P.; Han, C.; Wei, D.; Shen, Y. Synthesis of ZnO Nanowires / Au Nanoparticles Hybrid by a Facile One- Pot Method and Their Enhanced NO 2 Sensing Properties. *J. Alloys Compd.* **2019**, *783*, 503–512.

(4)   Gaiardo, A.; Fabbri, B.; Giberti, A.; Guidi, V.; Bellutti, P.; Malagù, C.; Valt, M.; Pepponi, G.; Gherardi, S.; Zonta, G.; et al. ZnO and Au/ZnO Thin Films: Room-Temperature Chemoresistive Properties for Gas Sensing Applications. *Sensors Actuators B. Chem.* **2016**.

(5)   Gogurla, N.; Sinha, A. K.; Santra, S.; Manna, S.; Ray, S. K. Multifunctional Au-ZnO Plasmonic Nanostructures for Enhanced UV Photodetector and Room Temperature NO Sensing Devices. *Sci. Rep.* **2014**, *4* (September).

(6)   Mun, Y.; Park, S.; An, S.; Lee, C.; Woo, H. NO_2 Gas Sensing Properties of Au-Functionalized Porous ZnO Nanosheets Enhanced by UV Irradiation. *Ceram. Int.* **2013**, No. 2, 1–8.

(7)   Rai, P.; Kim, Y. S.; Song, H. M.; Song, M. K.; Yu, Y. T. The Role of Gold Catalyst on the Sensing Behavior of ZnO Nanorods for CO and NO 2 Gases. *Sensors Actuators, B Chem.* **2012**, *165* (1), 133–142.